Renormalized dispersing multiplets in the spectrum of nearly Mott localized systems

Yashar Komijani,[1,*] Karen Hallberg,[2] and Gabriel Kotliar[1]
[1]*Department of Physics and Astronomy, Rutgers University, Piscataway, New Jersey 08854, USA*
[2]*Centro Atómico Bariloche and Instituto Balserio, CNEA and CONICET, 8400 Bariloche, Argentina*

(Received 17 October 2018; revised manuscript received 17 January 2019; published 27 March 2019)

The spectrum of the strongly correlated systems usually shows resonant peaks at finite energy, with examples in the 115 Ce family which are reproduced by the dynamical mean-field theory. A similar structure has been seen recently in the orbitally selective Mott phase of the two-band model, known as the doublon-holon bound state, with implications for the fate of such phase in the zero Hund's coupling limit. We show that these features can be captured with the slave-particle methods once their Hilbert space is taken into account. We use slave-spin calculations, justifiable in the limit of large dimensions, to explicitly demonstrate this and compare the results with dynamical mean-field theory.

DOI: 10.1103/PhysRevB.99.125150

I. INTRODUCTION

The study of the properties of quantum materials, including high-temperature superconductors, requires understanding strongly correlated systems in two or three dimensions, a task which is theoretically very challenging. Dynamical mean-field theory (DMFT) [1], one of the very few tools at our disposal, provides a systematic interpolation between the atomic limit where the correlations are important and the noninteracting limit of band theory, and is exact in the limit of infinite dimensions. However, analytical insight into the result is often formidable as a result of the self-consistency loop.

There have been lots of efforts to produce analytically tractable understanding using slave-particle mean-field theories [2–7]. While when treated exactly all these methods in principle agree, the approximation schemes used for analytical/numerical tractability cause discrepancies, for example for the fate of the so-called orbitally selective Mott (OSM) phase in the absence of Hund's coupling, which has been a source of confusion. The simplest version of the phenomena appears in a two-band Hubbard model with orbital-dependent tunneling and local interaction. Slave-spin methods [4,8] predict that when the ratio of the bandwidths of the two bands $r = t_2/t_1$ is close to one, the two bands undergo a transition between Mott phase and the metallic phase at the same value of Hubbard U, the so-called *locking effect*, whereas when the bandwidth ratio is smaller than a threshold of about $r_c = 0.2$, there is a region of the OSM phase in the phase diagram in which one band is metallic and the other band is itinerant. This agrees with some [4] and disagrees with other DMFT calculations [9–12]. Moreover, the general consensus is that Hund's coupling J_H favors the OSM phase and decreases r_c.

In a recent study, some of us [13,14] used a density-matrix renormalization group (DMRG) impurity solver [15] to obtain very accurate DMFT results on the two-orbital problem. In the absence of a Hund's interaction, Núñez Fernández *et al.* [13] found locking, irrespective of the ratio of the bandwidths. Moreover, when including an interorbital Coulomb interaction U_{12}, they identified a resonant feature in the spectral function of the localized orbital in the OSM phase, dubbed the *holon-doublon* excitonic peak corresponding to a virtual bound state at energy scales of about $\Delta = U - U_{12}$. Additionally, the two-site, two-orbital model studied in [13] shows that this bound state corresponds to the empty state in one orbital and double occupancy of the other orbital at the same site or vice versa. This is different from previous studies of holon-doublon peaks in the single-band Hubbard model [16–18] where, due to the limited size of the local Hilbert space, the holon-doublon bound state necessarily forms between nearby sites.

The problem of understanding the origin of finite-energy multiplets in the spectrum of the strongly correlated quantum materials [19,20] is general and not limited to the two-orbital case mentioned above. Here, we show that slave-particle mean-field methods are fully capable of capturing these finite-energy spectral features, and in particular, the holon-doublon peak. Similar methods have been applied in the past to analyze the spectrum of mixed valence compounds, including Pu pnictides and chalcogenides [21] and the 115 Ce family: $CeIrIn_5$, $CeCoIn_5$, and $CeRhIn_5$ [22].

The structure of the paper is the following: In Sec. II, we describe the general formalism of the method, as well as various approximation schemes. Section III applies the general method of Sec. II to study the spectral functions of single- and two-band lattices, including the holon-doublon bound state, using the Z_2 slave-spin method. In Sec. IV we compare numerical results from the slave-spin method to DMFT. Appendix A contains a comparison between exact diagonalization and the slave-spin method applied to the two-orbital two-site problem. Appendixes B and C contain diagonalization of the slave-spin Hamiltonian and the spectral representation of the slave-particle Green's function, respectively.

*komijani@physics.rutgers.edu

II. GENERAL FORMALISM

We consider tight-binding models with the general Hamiltonian

$$H = \sum_{\langle ij\rangle\alpha\beta} t_{\alpha\beta} d^\dagger_{i\alpha} d_{j\beta} + \sum_j H_{int}[j], \tag{1}$$

where $d^\dagger_{i\alpha}$ creates an electron of spin/orbital α at site i of the lattice and the interaction $H_{int}[j]$ is assumed to be local, expressed in terms of $d^\dagger_{j\alpha}$ and $d_{j\beta}$ only, but otherwise general. In slave-particle methods we introduce a parton construction for the fermionic operator $d_{j\alpha} = \hat{z}_{j\alpha} f_{j\alpha}$, where $\hat{z}_{j\alpha}$ has its own Hilbert space (without loss of generality we restrict our discussion to the simpler cases in which z and f share the same index). As a result, the Hilbert space is enlarged to the tensor product of that of the f and z particles, which is larger than the original Hilbert space by the gauge transformations that leave the physical operators invariant. Correlation functions of $d_{j\alpha}$ are gauge-invariant and can be studied using a representative slave-particle state $|\Phi_0\rangle = |f_{j\alpha}\rangle|\hat{z}_{j\alpha}\rangle$ [23]. A constraint (usually imposed on average via a few Lagrange multipliers) ensures that the averaged physical parameters are computed in the originally restricted part of the extended Hilbert space. The real advantage is that the constraints can be used to express $H_{int}[j]$ entirely in terms of slave-particle $\hat{z}$ variables. As a next step the Hamiltonian (1) is mean-field decoupled into $H_{MF} = H_f + H_z$, where

$$H_z = \sum_{\langle ij\rangle\alpha\beta} J^{\alpha\beta}_{ij} \hat{z}^\dagger_{i\alpha} \hat{z}_{j\beta} + \sum_i H_{int}[i] \tag{2}$$

and

$$H_f = \sum_{\langle ij\rangle\alpha\beta} \tilde{t}^{\alpha\beta}_{ij} f^\dagger_{i\alpha} f_{j\beta} \tag{3}$$

with the parameters given by

$$\tilde{t}^{\alpha\beta}_{ij} = t^{\alpha\beta}_{ij} \langle \hat{z}^\dagger_{i\alpha} z_{j\beta}\rangle, \quad J^{\alpha\beta}_{ij} = t^{\alpha\beta}_{ij} \langle f^\dagger_{i\alpha} f_{j\beta}\rangle. \tag{4}$$

Here, H_f describes the renormalized fermionic bands, whereas H_z describes renormalized atomic structure. Using the constraints, $H_{int}[i]$ can be entirely absorbed into H_z. The ordered (disordered) phases of the z lattice are usually associated with itinerant (Mott-localized) phases of the original electrons. Note that H_{MF} breaks gauge symmetry, but can be used to give approximate expression for $|\Phi_0\rangle$.

The mean-field decoupling mentioned above neglects fluctuations in time that couple H_f and H_z, whereas these fluctuations are captured in DMFT. On the other hand long-wavelength spatial fluctuations are present in Eq. (2) and absent in single-site DMFT. However, Eq. (2) is still a many-body spin-lattice problem which can be studied numerically, and except for special symmetric cases [24] difficult to treat analytically. In practice, in order to solve the resulting interacting Hamiltonian in H_z one uses a single-site approximation, so that H_z is transformed to

$$H_{z,ss} = \sum_\alpha (h_\alpha \hat{z}^\dagger_\alpha + \text{H.c.}) + H_{int}, \quad h_\alpha = \sum_{j\beta} J^{\alpha\beta}_{ij} z_\beta, \tag{5}$$

where $z_\beta \equiv \langle \hat{z}_{j\beta}\rangle$ and we have used that due to translational invariance h_α and z_α are independent of position. Equations (2)–(5) provide a closed set of equations that can be solved for z_α. The spatial correlations are lost in this process, similarly to the single-site DMFT. Systematic approaches to improve this result have been achieved by (i) cluster extensions [3,25] or (ii) long-wavelength magnon-like excitations [23].

An energetic competition between these H_f and $H_{z,ss}$ leads to itineracy or localization. Using the assumption of the mean-field decoupling between z-s and f-s, the single-particle Green's function $G_{d,\alpha\beta}(j,\tau) = \langle -T d_{j\alpha}(\tau) d^\dagger_{0\beta}\rangle$, with site index j and imaginary time τ, can be written

$$G_{d,\alpha\beta}(j,\tau) = \Pi_{\alpha\beta}(j,\tau) G_{f,\alpha\beta}(j,\tau), \tag{6}$$

where $G_{f,\alpha\beta}(j,\tau) = \langle -T f_{j\alpha}(\tau) f^\dagger_{0\beta}\rangle$ and $\Pi_{\alpha\beta}(j,\tau) = \langle T \hat{z}_{j\alpha}(\tau) \hat{z}^\dagger_{0\beta}\rangle$. Within the single-site approximation, $\langle z_{i\alpha}(\tau) z^\dagger_{j\beta}\rangle = \langle z_{i\alpha}(\tau)\rangle \langle z_{j\beta}{}^\dagger\rangle$ for $i \neq j$, so that we can write

$$\Pi_{\alpha\beta}(j,\tau) = \begin{cases} Z_{\alpha\beta}, & j \neq 0, \\ \Pi_{\alpha\beta}(\tau), & j = 0, \end{cases} \tag{7}$$

where $Z_{\alpha\beta} = z_\alpha z^*_\beta$. Without lack of generality, in the following we restrict the discussion to the diagonal $\alpha = \beta$ elements. The function $\Pi_{\alpha\alpha}(\tau)$ "knows" about the renormalized atomic physics as seen from its spectral representation

$$\Pi_{\alpha\alpha}(i\nu_p) = e^{-\Omega/T} \sum_{nm} \frac{e^{-E_n/T} - e^{-E_m/T}}{i\nu_p + E_n - E_m} |\langle n|\hat{z}_\alpha|m\rangle|^2, \tag{8}$$

where T is the temperature, $\nu_p = 2\pi pT$ are Matsubara frequencies, and Ω is the Gibbs free energy. This atomic structure in $\Pi(\tau)$ is reflected in G_d after convolution with the renormalized dispersing band G_f. If the renormalized band is narrow enough (at, or close to, a partial Mott transition), the atomic features of the G_d can be resolved, whereas in the metallic regime usually G_f is broad and those features are washed out after convolution. We use this method to show that various (renormalized) atomic multiplets can be identified in the complex many-body spectrum of the multichannel Hubbard model. In addition to the bare atomic orbitals, this contains additional multiplets arising due to an interplay between Mott localization in one band and itineracy in the other band [13]. We demonstrate this explicitly, by comparing slave-particle methods to the solution of a two-site problem considered before [13] and then generalizing to the lattice.

Inserting (7) in (6) and going to momentum space,

$$G_{d,\alpha\beta}(k,\tau) = Z_{\alpha\beta} G_{f,\alpha\beta}(k,\tau) + [\Pi_{\alpha\beta}(\tau) - Z_{\alpha\beta}] \sum_q G_{f,\alpha\beta}(q,\tau); \tag{9}$$

i.e., G_d contains a k-dependent part coming from renormalized noninteracting band G_f plus some k-independent atomic structure in the last term. In particular in the Mott phase $Z = 0$ no k dependence exists. The atomic multiplets are obviously not dispersing in this expression, a consequence of the single-site approximation in Eq. (5) reflected in the local form of the dynamical part of $\Pi_{\alpha\beta}(j,\tau)$ in Eq. (7). A more accurate treatment of spatial correlations in Eq. (2) is expected to lead to dispersing multiplets.

A second point of this paper is that the two limits of mean-field decoupling and single-site approximation generally do not commute with each other. This is schematically

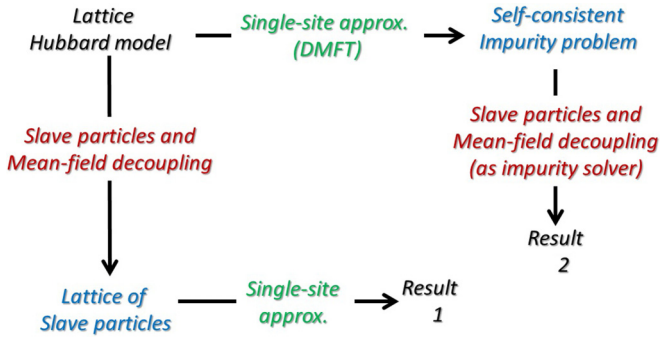

FIG. 1. A representation of noncommutativity of the two approximations: mean-field decoupling and single-site approximation.

represented in Fig. 1. To see this, consider doing a single-site approximation first. This is achieved by the single-site DMFT, according to which the lattice problem is mapped to an effective impurity problem embedded within a conduction bath:

$$H_{imp} = \sum_{k\alpha\beta}(V_{k\alpha\beta}d^\dagger_\alpha c_{k\beta} + \text{H.c.}) + H_{int} + H_c, \tag{10}$$

where $H_c = \sum_{k\alpha}\epsilon_{k\alpha}c^\dagger_{k\alpha}c_{k\alpha}$ and the hybridization function $\Delta(z) = \sum_k |V_{k\alpha\beta}|^2/(z-\epsilon_k)$ is chosen so that locally, the Green's functions of the lattice and impurity are equal:

$$G_{loc}(z) \equiv \sum_k G_{lat}(k,z) = G_d(z). \tag{11}$$

The impurity problem is solved first. Extracting $\Sigma_I(z)$ from the $G_d^{-1}(z) = z - \Delta(z) - \Sigma_I(z)$, and assuming $\Sigma_{lat}(k,z) = \Sigma_I(z)$ is local, the lattice Green's function $G(k,z) = [z - \epsilon_k - \Sigma_I(z)]^{-1}$ is computed. From this and Eq. (11), a new hybridization function $\Delta(z)$ is extracted and the loop is repeated until convergence is reached.

The slave-particle methods can be used as an impurity solver for this DMFT loop. The resulting Hamiltonian

$$H_{imp} = \sum_{k\alpha\beta}(V_{k\alpha\beta}\hat{z}^\dagger_\alpha f^\dagger_\alpha c_{k\beta} + \text{H.c.}) + H_{int}\{\hat{z}_\alpha\} + H_c \tag{12}$$

is still interacting. Various approximate schemes exist to solve this impurity problem, including the noncrossing approximation (NCA) [26,27] and one-crossing approximation (OCA) [27]. For the purpose of studying multiplets and the comparison to the mean-field solution above, it suffices to settle on a mean-field decoupling. As a result, Eq. (12) gives $H_{imp} = H_{imp,f} + H_{z,ss}$, where $H_{z,ss}$ is the same as in Eq. (5), except that the expression for h_α is modified to

$$h_\alpha = \sum_{k\beta} V_{k\alpha\beta}\langle f^\dagger_\alpha c_{k\beta}\rangle, \tag{13}$$

and $H_{imp,f}$ is given by

$$H_{imp,f} = \sum_{k\alpha\beta}(\tilde{V}_{k\alpha\beta}f^\dagger_\alpha c_{k\beta} + \text{H.c.}) + \sum_{k\alpha}\epsilon_{k\alpha}c^\dagger_{k\alpha}c_{k\alpha}, \tag{14}$$

where $\tilde{V}_{k\alpha\beta} = V_{k\alpha\beta}z^*_\alpha$. The impurity Green's function is then

$$G_{f,\alpha\beta}(z) = \frac{1}{z - \tilde{\Delta}_{\alpha\beta}(z)}, \quad G_{d,\alpha\beta}(\tau) = \Pi_{\alpha\beta}(\tau)G_{f,\alpha\beta}(\tau). \tag{15}$$

It is clear that even though $G_d(\tau)$ is factorizable, in this scheme $G_{lat}(k,\tau)$ does not factorize, as opposed to (6), and consequently the multiplets are generally dispersing. Another manifestation of the noncommutativity of the two approximations is difference in Z computed from the two approaches. We present a comparison of the two approaches for the single-orbital case in the next section.

It is noteworthy that under the commonly used simplification $\Pi(n,\tau) \approx Z$, then $\Sigma_I(z) = \Sigma_{lat}(z) = (1-Z)z$ and the two approximation schemes discussed above are equivalent as can be shown explicitly [8]. But the multiplets (the central focus of this paper) would be lost in this approximation.

In the Kotliar-Ruckenstein four-boson method [2] or in rotationally invariant slave bosons [3], the bosons are condensed (treated as c-numbers) at zero temperature, which is another (third) level of approximation, equivalent to $\Pi(n,\tau) \approx Z$ mentioned above. Since the time dependence of $\Pi(\tau)$ is lost in this process, no atomic multiplet shows up in the spectra. Gaussian corrections to the condensate simultaneously (a) retrieve the Hilbert space of bosons and (b) account for spatial and (c) temporal fluctuations mentioned before.

III. Z_2 SLAVE-SPIN MEAN FIELD

The above discussion was general. In this section, we focus on the Z_2 slave-spin method [4], where at half filling $\hat{z}_\alpha = \tau^x_\alpha$ and the constraint $2f^\dagger_\alpha f_\alpha = \tau^z_\alpha + 1$ is applied on average, via a Lagrange multiplier λ_α. Here τ^a_α with $a = x, y, z$ are Pauli matrices that square to 1. Due to particle-hole symmetry, these Lagrange multipliers vanish $\lambda_\alpha = 0$ at the saddle point [8].

The fact that the $U(1)$ charge is carried by the f_α in this method indicates that as long as $\tilde{t}_{ij} = t_{ij}\langle\tau^x_i\tau^x_j\rangle$ is nonzero (even if $\langle\tau^x\rangle = 0$) the bulk is conducting and the system is not in a Mott phase [28]. Therefore, we only consider the limit of large dimensions where the single-site approximation is valid, the relation $\langle\tau^x_i\tau^x_j\rangle = \langle\tau^x\rangle^2$ is satisfied, and $\langle\tau^x\rangle = 0$ is equivalent to Mott localization [8,29].

A. Single band

In the single-band case, the Hamiltonian has the general impurity form of Eq. (10) with $\alpha = \uparrow, \downarrow$ and the interaction $H_{int} = U\tilde{n}_\uparrow\tilde{n}_\downarrow$, where $\tilde{n}_\sigma = d^\dagger_\sigma d_\sigma - 1/2$. Using the slave-spin method we identify $\tilde{n}_\sigma = \tau^z_\sigma/2$, so that

$$H_{z,ss} = a_\uparrow\tau^x_\uparrow + a_\downarrow\tau^x_\downarrow + U\tau^z_\uparrow\tau^z_\downarrow, \tag{16}$$

where $a_\sigma = 2h_\sigma = 2\mathcal{J}z_\sigma$ and $\mathcal{J} = -0.212D$ is the average kinetic energy for a Bethe lattice of bandwidth $D = 2t$. A better choice of basis is

$$|\psi^\pm_1\rangle = \frac{|\Uparrow_\uparrow \Downarrow_\downarrow \pm \Downarrow_\uparrow\Uparrow_\downarrow\rangle}{\sqrt{2}}, \quad |\psi^\pm_2\rangle = \frac{|\Uparrow_\uparrow \Uparrow_\downarrow \pm \Downarrow_\uparrow\Downarrow_\downarrow\rangle}{\sqrt{2}}. \tag{17}$$

Here, $|\Uparrow_\sigma\rangle$ or $|\Downarrow_\sigma\rangle$ refers to the eigenstates of the τ^z_σ operator, where $\sigma = \uparrow, \downarrow$. In the paramagnetic regime

$a_\uparrow = a_\downarrow = a$. Due to particle-hole symmetry $|\psi^-_{1,2}\rangle$ decouples and in the basis of $|\psi^+_{1,2}\rangle$ the Hamiltonian reduces to $H_{z,ss} = \alpha\tau^x + (U/4)\tau^z$ with $\alpha = 2a$. This two-state problem can be diagonalized with an $SO(2)$ rotation

$$\begin{pmatrix}|\psi_g\rangle\\|\psi_e\rangle\end{pmatrix} = \begin{pmatrix}\cos\theta & \sin\theta\\ -\sin\theta & \cos\theta\end{pmatrix}\begin{pmatrix}|\psi^+_1\rangle\\|\psi^+_2\rangle\end{pmatrix}, \tag{18}$$

where $\tan 2\theta = 2\alpha/(E_2 - E_1)$ and the eigenenergies are

$$E_{g/e} = U/4 \mp \sqrt{(U/4)^2 + \alpha^2}. \tag{19}$$

Note that $E_g(\alpha \to 0) \approx -2\alpha^2/U$. The mean-field study of this problem has been discussed in the past [4,8,30]. In the case of the Hubbard model, $z_\sigma = \langle\psi_g|\tau^x_\sigma|\psi_g\rangle = \sin 2\theta$. By minimizing the free energy, it can be shown that $Z \equiv |z_\sigma|^2 = \sin^2 2\theta$ follows the Brinkman-Rice theory [31] $Z = [1-u^2]\theta(1-u)$, where $\theta(x)$ is the Heaviside step function, $u = U/U_c$, and $U_c = 16|\mathcal{J}| = 3.36 \times 2t$.

In the case of an Anderson impurity, $Z = |z_\sigma|^2$ plays the role of an "order parameter" for the Kondo physics. The relation between a_σ and z_σ in Eq. (16) in this case can be extracted from Eq. (13) or a minimization of the free energy $F = F_f + F_z(a) - 2az$, and is given by [8]

$$a_\alpha = -\frac{2}{z_\alpha}\int \frac{d\omega}{\pi} f(\omega)\mathrm{Im}\big[G^{\alpha\alpha}_f(\omega + i\eta)\big]. \tag{20}$$

In both cases, the function $\Pi(\tau)$ at low temperature is equal to

$$\Pi(\tau) = \langle T\tau^x_\uparrow(\tau)\tau^x_\uparrow\rangle = Z + (1-Z)e^{-|\tau|\Delta E}, \tag{21}$$

where $\Delta E = E_e - E_g$ and $Z = \sin^2(2\theta_g)$. Multiplying by $G_f(\tau)$ and Fourier transforming,

$$\begin{aligned} G''_d(\omega) = ZG''_f(\omega) + (1-Z)[&G''_f(\omega+\Delta E)\theta(\omega < -\Delta E)\\ &+ G''_f(\omega-\Delta E)\theta(\omega > \Delta E)]. \end{aligned} \tag{22}$$

Here, $\theta(\omega)$ appears as a low-temperature limit of $f(\omega \pm \Delta E) + n_B(\pm\Delta E)$ (Appendix C). The real part $G'_d(\omega)$ follows from Eq. (22) using Hilbert transform.

On a Bethe lattice of bandwidth $2t$ with density of states $\rho(\epsilon) = (\pi t)^{-1}\sqrt{1-(\epsilon/2t)^2}$, we can plot the spectrum as a function of frequency ω and the Bethe lattice energy ϵ. Figure 2 shows a comparison between the (ϵ-resolved and integrated) spectral function, as computed from Eq. (22) with a Brinkman-Rice Z and a lattice G_f, vs a DMFT calculation with a slave-spin impurity solver where G_f is the Green's function of the impurity. Overall, the two results look quite similar. Note that the Hubbard bands are featureless in (a) but disperse in (c) and there are slight differences in Z. From this and the sum rules we expect the integrated area of the Hubbard peaks to be similar in the two approaches; however more has to be done to understand the similarity in their widths.

Since we do not have access to the exact many-body result, an unbiased assessment of the relative accuracy of result 1 vs result 2 is beyond the scope of this work. However, close to the Mott transition, slave spins behave poorly as the impurity solver for DMFT due to the fact that $\Delta(z) = z - \Sigma_I - G^{-1}_{loc}$ is nonanalytical, the so-called noncausality of the impurity solver, which limits the practicality of the approach 2. Moreover, the necessity of a numerical implementation of the Hilbert transform obscures the analytical tractability of the method in the second approach. Therefore, in the following we use the analytical approach 1 and compare it to a DMFT study with an exact impurity solver.

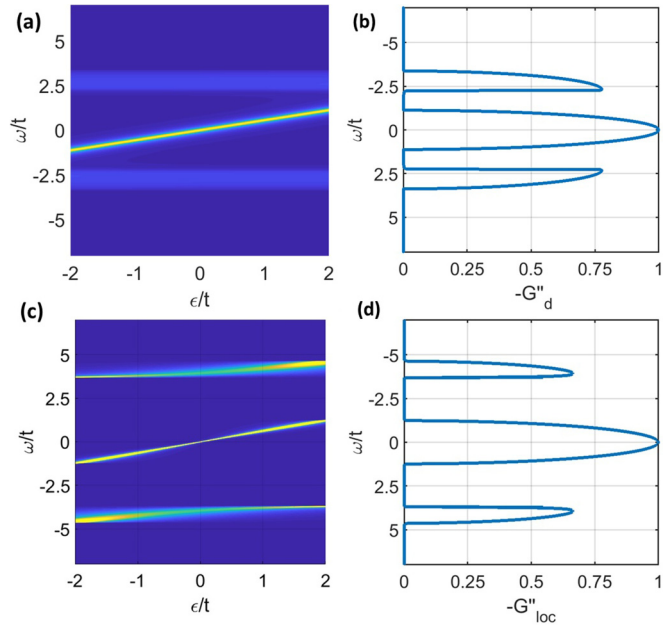

FIG. 2. A comparison of results 1 and 2 of Fig. 1 for a single-band system at $U = 4.5t$. (a) The slave-spin mean-field spectral function $-G''(\epsilon, \omega + i\eta)$ as a function of frequency and the Bethe lattice energy ϵ. (b) The local spectral function, with $Z = 0.56$. (c) The result of using slave spins as the impurity solver for DMFT which gives $Z = 0.63$. (d) The local spectral function from DMFT.

B. Two-band model

In the two-band model, the impurity problem is given by Eq. (10) with $\alpha = 1\uparrow, 1\downarrow, 2\uparrow, 2\downarrow$. To make a connection to Ref. [13] we choose the same form of simplified interaction,

$$\begin{aligned} H_{int} &= U\sum_i\sum_{m=1}^{2}\tilde{n}_{im\uparrow}\tilde{n}_{im\downarrow} + U_{12}\sum_i\sum_{\sigma\sigma'=\uparrow,\downarrow}\tilde{n}_{i1\sigma}\tilde{n}_{i2\sigma'}\\ &= \sum_i\Big\{\frac{U}{2}(\tilde{n}_{i1\uparrow}+\tilde{n}_{i1\downarrow}+\tilde{n}_{i2\uparrow}+\tilde{n}_{i2\downarrow})^2 - \frac{U}{2}\\ &\quad - \Delta(\tilde{n}_{i1\uparrow}+\tilde{n}_{i1\downarrow})(\tilde{n}_{i2\uparrow}+\tilde{n}_{i2\downarrow})\Big\}, \end{aligned} \tag{23}$$

where $\tilde{n}_\alpha \equiv n_{f\alpha} - 1/2$ and $\Delta = U - U_{12}$ is the difference between the intra- and interorbital Coulomb couplings. We will drop the $-U/2$ constant term in the following. While this form of the interaction is simpler to follow, we have obtained qualitatively similar results with a more general Kanamori Hamiltonian.

Within the slave-spin method this becomes

$$H_{z,ss} = \sum_{m\sigma} a_{m\sigma}\tau^x_{m\sigma} + H_{int}\big[\tilde{n}_\alpha \to \tau^z_\alpha\big]. \tag{24}$$

As before, $a_{m\sigma} = 2\mathcal{J}_m z_{m\sigma}$ and $\mathcal{J}_m \propto D_m$ and in the paramagnetic regime, $a_{m\sigma} = a_m$ and $z_{m\sigma} = z_m$. The Hamiltonian is a

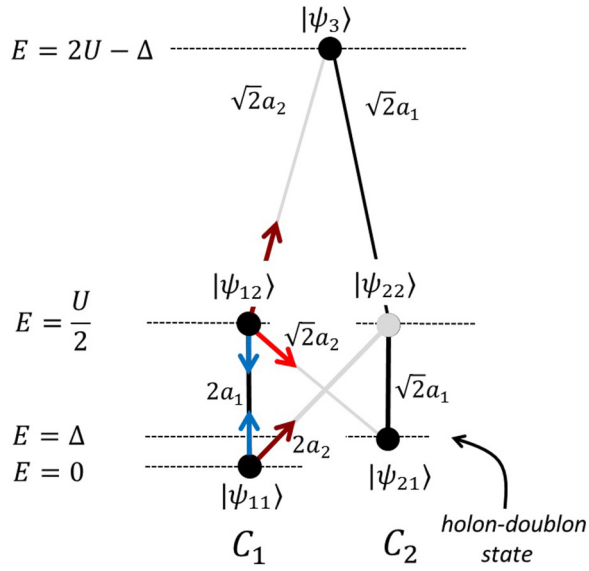

FIG. 3. The relevant sector of the slave-spin Hamiltonian (see Appendix B), with states given in Eqs. (25). The black circles represent atomic states at the atomic energies, corresponding to the diagonal part of the slave-spin Hamiltonian. The quantities $2a_1$, $2a_2, \ldots$ represent the off-diagonal elements of the slave-spin Hamiltonian coupling the atomic states, as a result of which the eigenstates will shift accordingly. At OSM phase $a_2 = 0$, and the Hamiltonian breaks into C_1 and C_2 sectors, with the ground state in sector C_1 due to larger level repulsion and lower energies. The transitions caused by $\tau^x_{1\sigma}$ and $\tau^x_{2\sigma}$ are indicated by blue and red arrows, respectively. The bright red arrow is to the holon-doublon bound state $|\psi_{21}\rangle$.

16×16 matrix, and the full calculation of the wave functions, eigenenergies, and correlation functions $\Pi_{11}(\tau)$ and $\Pi_{12}(\tau)$ is done numerically.

Here in order to get an analytical insight, we rather make a simplifying assumption that the system is already in an OSM regime, $a_2 = 2\mathcal{J}_2 z_2 = 0$. As a result, the relevant sectors of the Hamiltonian (Appendix B), shown diagrammatically in Fig. 3, break into two 2×2 matrix blocks with level repulsion $\alpha_1 = 2a_1$ and $\alpha_2 = \sqrt{2}a_1$. The vertical axis is the energy. The diagonal elements of the matrix are represented by black/gray dots and the off-diagonal matrix elements are represented by the black/gray lines connecting the dots. The basis and the diagonal energies are

$$
\begin{aligned}
|\psi_{11}\rangle &= \frac{|\Uparrow_\uparrow \Downarrow_\downarrow + \Downarrow_\uparrow \Uparrow_\downarrow\rangle_1}{\sqrt{2}} \frac{|\Uparrow_\uparrow \Downarrow_\downarrow + \Downarrow_\uparrow \Uparrow_\downarrow\rangle_2}{\sqrt{2}}, \quad E_{11} = 0, \\
|\psi_{21}\rangle &= \frac{|\Uparrow_\uparrow \Uparrow_\downarrow\rangle_1 |\Downarrow_\uparrow \Downarrow_\downarrow\rangle_2 + |\Downarrow_\uparrow \Downarrow_\downarrow\rangle_1 |\Uparrow_\uparrow \Uparrow_\downarrow\rangle_2}{\sqrt{2}}, \quad E_{21} = \Delta, \\
|\psi_{12}\rangle &= \frac{|\Uparrow_\uparrow \Uparrow_\downarrow + \Downarrow_\uparrow \Downarrow_\downarrow\rangle_1}{\sqrt{2}} \frac{|\Uparrow_\uparrow \Downarrow_\downarrow + \Downarrow_\uparrow \Uparrow_\downarrow\rangle_2}{\sqrt{2}}, \quad E_{12} = \frac{U}{2}, \\
|\psi_{22}\rangle &= \frac{|\Uparrow_\uparrow \Downarrow_\downarrow + \Downarrow_\uparrow \Uparrow_\downarrow\rangle_1}{\sqrt{2}} \frac{|\Uparrow_\uparrow \Uparrow_\downarrow + \Downarrow_\uparrow \Downarrow_\downarrow\rangle_2}{\sqrt{2}}, \quad E_{22} = \frac{U}{2}, \\
|\psi_3\rangle &= \frac{|\Uparrow_\uparrow \Uparrow_\downarrow\rangle_1 |\Uparrow_\uparrow \Uparrow_\downarrow\rangle_2 + |\Downarrow_\uparrow \Downarrow_\downarrow\rangle_1 |\Downarrow_\uparrow \Downarrow_\downarrow\rangle_2}{\sqrt{2}}, \quad E_3 = 2U.
\end{aligned}
\tag{25}
$$

In the following we assume that the fully empty/filled states $|\psi_3\rangle$ can be discarded. This is justified close to the Mott transition [8]. In terms of these, the eigenfunctions $j = 1, 2$ for the sector $i = 1, 2$ are

$$
\begin{pmatrix} |\tilde{\psi}_{i1}\rangle \\ |\tilde{\psi}_{i2}\rangle \end{pmatrix} = \begin{pmatrix} \cos\theta_i & \sin\theta_i \\ -\sin\theta_i & \cos\theta_i \end{pmatrix} \begin{pmatrix} |\psi_{i1}\rangle \\ |\psi_{i2}\rangle \end{pmatrix}, \tag{26}
$$

where $\tan 2\theta_i = 2\alpha_i/(E_{2i} - E_{1i})$ and the eigenenergies

$$
\tilde{E}_{ij} = \frac{E_{i1} + E_{i2}}{2} - \sigma_j \sqrt{[(E_{i1} - E_{i2})/2]^2 + \alpha_i^2}, \tag{27}
$$

where $\sigma_1 = -\sigma_2 = 1$. The level repulsions are $\alpha_1 = 2a_1$ and $\alpha_2 = \sqrt{2}a_1$. The ground state belongs to the sector $i = 1$. The correlation functions $\Pi_{ii}(\tau) \equiv \langle T\, \tau^x_{i\uparrow}(\tau) \tau^x_{i\uparrow} \rangle$ are then

$$
\begin{aligned}
\Pi_{11}(\tau) &= Z_1 + (1 - Z_1) e^{-|\tau|(\tilde{E}_{12} - \tilde{E}_{11})}, \\
\Pi_{22}(\tau) &= e^{-|\tau|(\tilde{E}_{21} - \tilde{E}_{11})} \sin^2(\theta_2 + \theta_1) \\
&\quad + e^{-|\tau|(\tilde{E}_{22} - \tilde{E}_{11})} \cos^2(\theta_1 + \theta_2),
\end{aligned}
\tag{28}
$$

where as before $Z_1 = \sin^2(2\theta_1)$.

1. Holon-doublon peaks in orbital-selective Mott phases

Equations (25) and (28) show that the lowest-energy intermediate state accessed by Π_{22} is the doublon-holon state $|\psi_{21}\rangle$. Whereas the other states are product states of two different orbitals, the doublon-holon state (as well as the high-energy state $|\psi_3\rangle$) is an entangled state of a doublon occupancy in either the first or second orbital and a holon in the other one.

This state is only accessible to the spectral function via the excited state $|\psi_{12}\rangle$, i.e., when the first (wider) band is metallic. It is instructive to study this effect on a two-site problem where one site is interacting and the other site plays the role of a noninteracting bath [13]. This is studied explicitly in Appendix A, and here we discuss the main result. Figure 4 shows the relevant sectors of a two-site Hamiltonian when $t_2 = 0$ (emulating Mott localization of the second band). The states of the impurity α_1 and α_2 and the bath β_1 are indicated in the form $|\alpha_1\alpha_2, \beta_1\rangle$. The blue and red arrows are the transitions caused by $d^\dagger_{1\sigma}$ and $d^\dagger_{2\sigma}$, respectively. The ground state is in the central sector and contains an admixture of the excited state due to the off-diagonal mixing $2t_1$. The spectral function of the first (delocalized) orbital, probed by the blue arrows, contains renormalized Hubbard peaks as well as a peak near zero frequency which would evolve into an Abrikosov-Suhl resonance when the number of bath sites increases [32]. The holon-doublon state $|02, 2\rangle$ is only accessible via the excited-state admixture (shown in bright red) and would disappear for $t_1 = 0$. In other words, in the fully atomic limit, $|02, 2\rangle$ is a dark state and is only visible when $t_1 \neq 0$.

The slave-spin method is capable of capturing the correlations discussed above in the two-site problem (Appendix A) as well as the DMFT results of Núñez Fernández *et al.* [13] for the Hubbard model. Within the single-site approximation, the Hamiltonian of the slave-spin sector is the same in all these cases [Eq. (24) and Fig. 3], while the mean values of the parameters a_1 and a_2 are different. The transitions probed by the $\tau^x_{2\sigma}$ in the slave-spin Hilbert space are marked by red in Fig. 3. The action of $\tau^x_{2\sigma}$ on $|\psi_{11}\rangle$ leads to $|\psi_{21}\rangle$ whereas

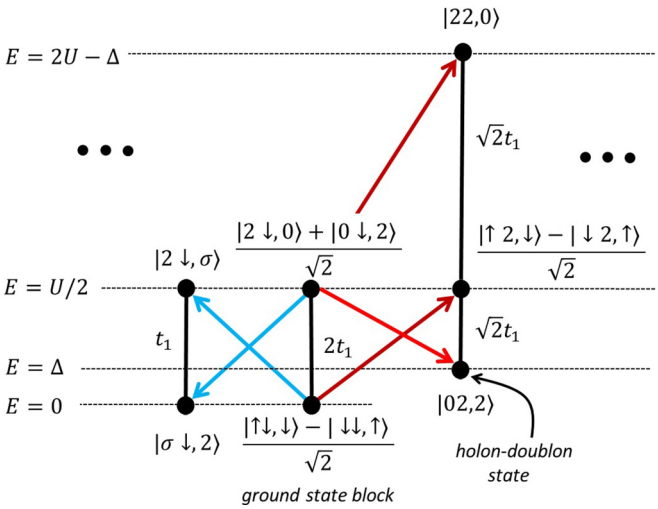

FIG. 4. Exact diagonalization of a two-site problem. The relevant sectors of the Hamiltonian of a two-orbital impurity with one bath site (Appendix A) when $t_2 = 0$. The states of the impurity α_1 and α_2 and the bath β_1 are indicated in the form $|\alpha_1\alpha_2, \beta_1\rangle$. Blue and red arrows indicate the transitions caused by $d^\dagger_{1\sigma}$ and $d^\dagger_{2\sigma}$, respectively. The bright red transition is to the holon-doublon state at energy Δ, only accessible from the ground state if t_1 is nonzero. The ellipses on the left and right indicate other sectors of the Hamiltonian, not involved in the ground state and not accessible with $d^\dagger_{1,2}$.

its acting on $|\psi_{12}\rangle$ leads to $|\psi_{22}\rangle$ (bright red). Therefore, only if the ground state contains an admixture of $|\psi_{12}\rangle$, i.e., when $\theta_1 \neq 0$ and the first band is metallic, does the holon-doublon state appear in the spectral function of the second orbital, or vice versa.

Assuming that the second orbital is in the Mott phase, in the impurity model $G_{f2}(\tau) = -\mathrm{sgn}\tau/2$, and in the lattice model $G_{f2}(n,\tau) = -\delta_{n0}\mathrm{sgn}\tau/2$. Multiplying by $\Pi_{22}(\tau)$ and Fourier transforming we find

$$2G_{d2}(\mathrm{z}) = \frac{\sin^2(\theta_2+\theta_1)}{\mathrm{z}-(\tilde{E}_{21}-\tilde{E}_{11})} + \frac{\cos^2(\theta_1+\theta_2)}{\mathrm{z}-(\tilde{E}_{22}-\tilde{E}_{11})} - (\mathrm{z}\to -\mathrm{z}). \tag{29}$$

The first term is the doublon-holon peak observed by the DMFT [13] in the spectrum of the narrow band in the OSM regime. The spectrum of the wider (itinerant) band is not affected and is essentially given by the results of previous section, Eq. (22), up to an enhancement of the effective Coulomb energy $U/2 \to U/2 + \Delta$ by the interorbital interaction.

2. Comparison with DMFT and discussion

Figure 5 compares the result of the calculation of the spectrum from the slave-spin method with that of DMRG+DMFT [13]. Figure 5(a) shows a comparison of the spectra in the OSM-phase regime in the presence of interorbital interaction $\Delta = 0.3$ and $t_2/t_1 = 0.5$. The incoherent broadening of the Hubbard peaks are not captured in the mean-field theory. However, a zoom into the low-frequency part in Fig. 5(b) shows that there is a good agreement on the position and the amplitude of the holon-doublon resonance between the two methods.

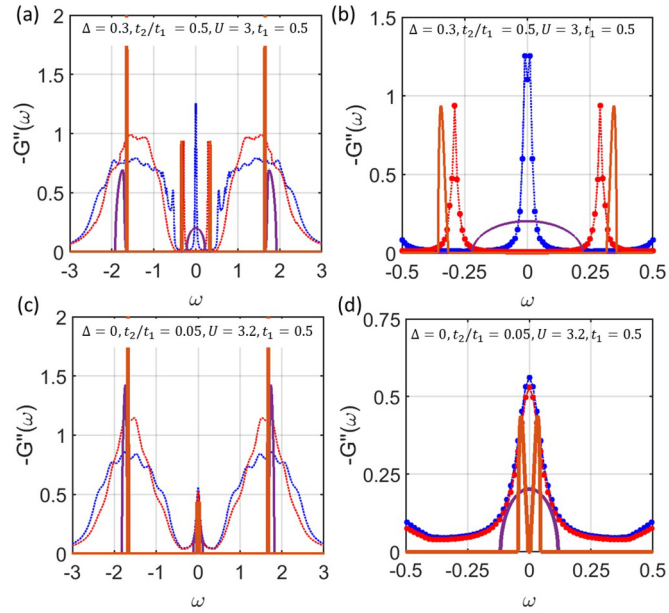

FIG. 5. A comparison of the spectral results between slave-spin mean field (continuous lines in dark color) and DMFT+DMRG (dashed lines without/with data points in left/right panels in bright color). The spectra of wider/narrower channels are shown in blue/red color. (a) In the presence of interorbital interaction $\Delta = 0.3$, $t_2/t_1 = 0.5$, $U = 3$, and $t_1 = 0.5$. (b) A zoom into the low-frequency part of (a). (c) No interorbital interaction $\Delta = 0$, $t_2/t_1 = 0.05$, $U = 3.2$, and $t_1 = 0.5$. (d) A zoom into the low-frequency part of (c).

In spite of the qualitative agreements for $\Delta \neq 0$, there are some disagreements for $\Delta = 0$ between slave-spin mean-field predictions and the DMFT+DMRG numerics. Figure 5(c) compares the spectra for $\Delta = 0$ and large anisotropy $t_2/t_1 = 0.05$. The slave-spin mean-field predicts the OSM phase in this regime, whereas DMFT predicts a finite Z. A zoom into the low-frequency part of the spectra in Fig. 5(d) shows that in contrast to the DMFT result, for $\Delta = 0$ the spectrum of the narrow band remains gapped and the wave-function renormalization remains zero [also Fig. 5(a)] in the mean-field solution.

The origin of this gap can be traced back to the pole $\mathrm{z} = \tilde{E}_{21} - \tilde{E}_{11}$ in Eq. (29). When $\Delta \to 0$, this gives

$$\mathrm{z} \to \sqrt{(U/4)^2 + 4a_1^2} - \sqrt{(U/4)^2 + 2a_1^2}. \tag{30}$$

If $a_1 \gg U$ this is at $\mathrm{z} = (2-\sqrt{2})a_1$ and for $a_1 \ll U$ is $\mathrm{z} \to 4a_1^2/U$, which linearly or quadratically depends on the width of the wider channel (or T_{K1} in the case of impurity). Therefore, the peak is expected to remain at finite frequency and follow the width of the coherent band in the wider channel.

Equations (28) and (29) show that although the total spectral weight of the two orbitals is equal to one, $\sin(2\theta_1) \neq \sin(\theta_1+\theta_2)$ and thus the weight of two holon-doublon peaks in the second orbital is not equal to the weight of the coherence band in the first orbital, in contrast to the observation of Ref. [13]. $\theta_i \in (0, \pi/4)$ quantifies the admixture of the high-energy state in the ground state of block i. For $\Delta/U \ll 1$, we have $\theta_2 < \theta_1$ and the coherence peak has higher spectral

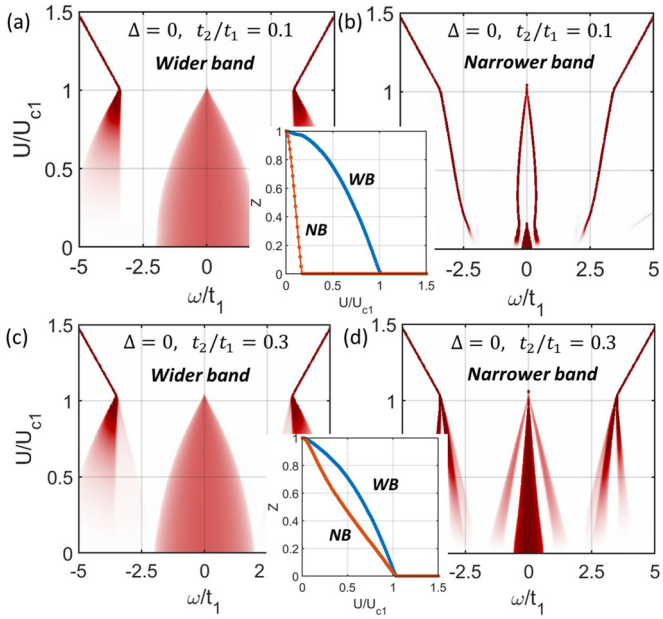

FIG. 6. The spectrum of the two bands in the absence of interorbital interaction $\Delta = 0$ from slave-spin mean-field method. (a), (b) OSM phase driven by bandwidth anisotropy and $t_2/t_1 = 0.1$. The middle inset shows the wave-function renormalizations vs U/U_{c1} for the first (blue) and second (red) bands. (c), (d) The locking regime $t_2/t_1 = 0.3$. The doublon-holon peaks develop into *bands* in the spectrum of the narrower band in addition to the coherence band. Middle inset: Wave-function renormalizations.

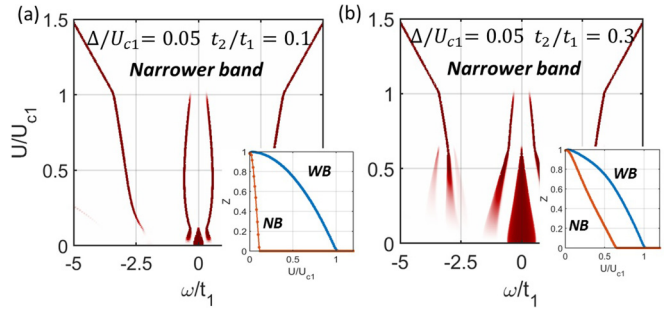

FIG. 7. The spectrum of the narrower band in the presence of interorbital interaction $\Delta = 0.05U_{c1}$ from slave-spin mean-field method: (a) $t_2/t_1 = 0.1$ and (b) $t_2/t_1 = 0.3$. OSM phase driven by bandwidth anisotropy and Δ. The insets shows the wave-function renormalizations vs U/U_{c1}.

weight than the doublon-holon peaks. But for $2\Delta/U > 1 - 1/\sqrt{2}$ this trend reverses.

When both bands are metallic, all five states mix to create various eigenstates. When a_2 is small, we can assume that the energies of $|\tilde{\psi}_{ij}\rangle$ are only slightly modified from the OSM-phase regime and $|\tilde{\psi}_{11}\rangle$ is still the ground state. However, the low-lying excited state $|\tilde{\psi}_{21}\rangle$ receives some admixture of $|\psi_{12}\rangle$ of $O(a_2)$. Therefore, $\langle\tilde{\psi}_{21}|\tau^x_{1\sigma}|\tilde{\psi}_{11}\rangle = O(a_2)$ is nonzero leading to the appearance of a weak resonance feature in the function $\Pi_1(z)$ at energy $\tilde{E}_{21}$. This feature is further weakened due to convolution with the coherence band $G_f(z)$ and appears as slight modulation of the coherence band in the wider orbital.

3. *Further numerical results from slave spin*

In this section, we summarize the numerical solution to the slave-spin mean-field equations. Figure 6 shows the evolution of quasiparticle peaks with Hubbard U for $\Delta = 0$, equivalent to zero Hund's coupling in the Kanamori-Hubbard model. Figures 6(a) and 6(b) show the case of $t_2/t_1 = 0.1$ which contains the OSM-phase regime (according to mean field). The wide-band spectrum shows the coherent peak as well as renormalized Hubbard peaks. In the narrow-band spectrum the coherent peak disappears at $U/U_{c1} \sim 0.2$ (top inset) while a doublon/holon resonant feature appears at $\omega/t_1 \sim 0.5$ which follows the evolution of the coherent band in the first (wider) orbital, and going to zero when the first orbital enters the Mott phase. Figures 6(c) and 6(d) show the case of $t_2/t_1 = 0.3$ which is the locking regime (bottom inset). The spectrum of the wide band is similar to before, but the narrow band is different in that (a) there is a coherent peak at $\omega \sim 0$. Instead of doublon-holon peak, we have a doublon-holon band whose splitting follows the width of the coherent band in the first orbital. There are additional fine structures in the Hubbard peaks in this case.

Figures 7(a) and 7(b) show the evolution of quasiparticle peaks in the narrower (second) band in presence of the interorbital interaction $\Delta/U_{c1} = 0.05$ for (a) $t_2/t_1 = 0.1$ and (b) $t_2/t_1 = 0.3$ with the wave-function renormalizations shown in the insets. The spectrum of the wider band is similar to the $\Delta = 0$ case. In both cases the doublon/holon quasiparticles are present but they disappear (at the Mott transition of the wider band) while their splitting is still finite.

IV. CONCLUSIONS

We have introduced a general formalism by which slave-particle methods capture atomic multiplets in the spectrum of nearly Mott localized orbitals. We studied the commutativity of the mean-field decoupling and single-site approximation, showing that the multiplets get renormalized and acquire dispersion within DMFT. We used slave spins and applied our formalism to reproduce the holon-doublon peak found in the DMFT results of Núñez Fernández *et al.* [13] for the two-band Hubbard model. Overall there is a good agreement between DMFT and slave-spin mean field. However, in contrast to DMFT, the splitting between holon-doublon peaks in slave-spin mean-field solution does not go to zero in the limit of zero Hund's coupling, in consistency with an OSM phase. This raises the question of whether quantum fluctuations beyond mean field can destroy the OSM phase in the absence of Hund's coupling, which we leave for the future.

ACKNOWLEDGMENTS

The authors are grateful to Y. Núñez Fernández for fruitful discussions, providing data, and an earlier collaboration, and also acknowledge stimulating discussions with P.-Y. Chang and T.-H. Lee. This work used XSEDE, which is supported by NSF Grant No. ACI-1548562. K.H. acknowledges support from Grant No. PICT 2016-0402 from the Argentine ANPCyT and PIP 2015-2017 (CONICET). G.K. was supported

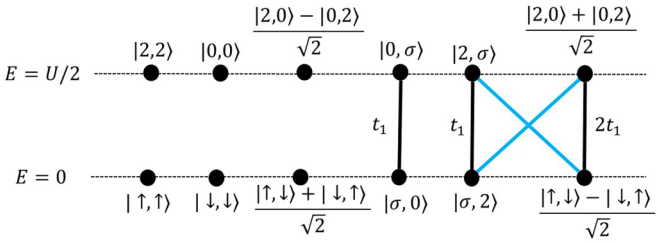

FIG. 8. A representation of the Hamiltonian in the single-orbital two-site problem. $|\alpha,\beta\rangle = |\alpha\rangle_d|\beta\rangle_c$ are the atomic states of the dot d and conduction site c, where $\alpha,\beta = 0,\uparrow,\downarrow,2$. Each atomic state is marked by a filled circle at the corresponding atomic energy. The black line denotes the transitions caused by tunneling, whereas the blue lines are transitions probed in the Green's function.

by NSF Grant No. DMR-1733071 and Y.K. was supported by a Rutgers University Materials Theory postdoctoral fellowship.

APPENDIX A: TWO-SITE PROBLEM

1. Single-orbital case

The Hamiltonian is $H = H_0 + H_T + H_c$, where

$$H_0 = \frac{U}{2}(n_\uparrow + n_\downarrow)^2, \quad H_T = \sum_\sigma (t d_\sigma^\dagger c_\sigma + \text{H.c.}). \tag{A1}$$

In the two site problem, at half filling we have $H_c = 0$. The Hamiltonian has $SU_{\text{charge}}(2) \otimes SU_{\text{spin}}(2)$ symmetry. Anticipating future symmetry-lowering additions, we use a smaller $U_{\text{charge}}(1) \otimes U_{\text{spin}}(1)$ symmetry to label states with Q^z and S^z. The distinct atomic states are denoted by filled circles at corresponding energy in Fig. 8, and the transition between them by H_T are marked in black. As a result, the Hamiltonian is block diagonal and the largest block is 2×2 corresponding to three two-level systems on the right of Fig. 8. Each group of atomic states connected by lines forms a block. The larger the off-diagonal element of the block, the larger is the level repulsion. Therefore, the ground state is given by the rightmost block:

$$E_g = U/4 - \sqrt{(U/4)^2 + 4t_1^2}, \tag{A2}$$

$$|\psi_g\rangle = \cos\theta_g \frac{|\uparrow,\downarrow\rangle + |\downarrow,\uparrow\rangle}{\sqrt{2}} + \sin\theta_g \frac{|2,0\rangle + |0,2\rangle}{\sqrt{2}} \tag{A3}$$

with $\theta_g = \tan^{-1}(E_g/2t_1)$. The Green's function is

$$G(\tau) = \langle -T d_\uparrow(\tau) d_\uparrow^\dagger(0)\rangle. \tag{A4}$$

At zero temperature and positive time $\tau > 0$ we have

$$G_D(\tau) \equiv G(\tau > 0) = -\langle \psi_g | e^{\tau H} d_\uparrow e^{-\tau H} \mathbb{1} d_\uparrow^\dagger | \psi_g\rangle. \tag{A5}$$

The blue lines in Fig. 8 show the transition caused by acting with $d_1^\dagger$ on the ground-state block. The result is creation of a "doublon" at the impurity site, which belongs to the second rightmost block. The intermediate states in $\mathbb{1}$ are

$$|\psi_\pm\rangle = \cos\theta_\pm |\sigma,2\rangle + \sin\theta |2,\sigma\rangle \tag{A6}$$

with the energies

$$E_\pm = U/4 \pm \sqrt{(U/4)^2 + t_1^2}, \tag{A7}$$

where $\theta_\pm = \tan^{-1}(E_\pm/t_1)$. Therefore, we find

$$G_d(\text{z}) = \frac{1}{2}\sum_{a=\pm}\left[\frac{\sin^2(\theta_g + \theta_\pm)}{\text{z} - (E_a - E_g)} - (\text{z} \to -\text{z})\right], \tag{A8}$$

where we used that the matrix element is given by $\langle \psi_a | d_\uparrow^\dagger | \psi_g\rangle = \sin(\theta_a + \theta_g)/\sqrt{2}$. This spectrum is composed of two resonances symmetric with respect to $\omega = 0$. The two energies have simple approximations in the limit of large U: one at $\sim t^2/U$ and the other at $\sim U/2$. The low-frequency resonance at $\omega = E_- - E_g$ is the single-bath site signature of the Abrikosov resonance peak (metallic regime), whereas the high-frequency resonance at $\omega = E_+ - E_g$ is the renormalized Hubbard peak.

Slave spin

It is remarkable that the same structure comes from the slave-spin method. After mean-field decoupling of slave spins and the quasiparticles we find $H = H_f + H_{z,ss} - 2az$, where $H_f = \sum_\sigma (\tilde{t} f_\sigma^\dagger c_\sigma + \text{H.c.})$ and $\tilde{t}_\sigma = z_\sigma t$. Diagonalizing H_f using molecular bonding/antibonding states we find

$$H = \tilde{t}(f_{+\sigma}^\dagger f_{+\sigma} - f_{-\sigma}^\dagger f_{-\sigma}), \quad \sqrt{2} f_\pm = f \pm c. \tag{A9}$$

The mean-field parameter z can be worked out from minimizing $F(a,z) = F_f + E_S(a_\sigma) - \Sigma_\sigma a_\sigma z_\sigma$. Eliminating a gives [8]

$$E_S = \frac{U}{4}\left[1 - \frac{1}{\sqrt{1-z^2}}\right] \tag{A10}$$

and

$$F(z) = F_f(z) - \frac{U}{4}[1 - \sqrt{1-z^2}]. \tag{A11}$$

In the present problem $F_f = -2_s t z$. Therefore,

$$z = [1 + (U/8t)^2]^{-1/2}. \tag{A12}$$

The Green's function $G_f(\tau) = \langle -T f(\tau) f^\dagger\rangle$ for $\tau > 0$ is

$$G_f(\tau) = -\frac{1}{2}\text{sgn}\tau e^{-\tilde{t}|\tau|}. \tag{A13}$$

Multiplying this by $\Pi(\tau)$ from Eq. (21) we find

$$G_d(z) = \frac{1}{2}\left[\frac{Z}{\text{z} - \tilde{t}} + \frac{1-Z}{\text{z} - (\tilde{t} + \Delta E)} - (\text{z} \to -\text{z})\right],$$

which again has the two peak structure we saw previously.

Figure 9 shows a comparison of the exact solution to the one obtained from the slave-spin method in the single-orbital two-site problem for $U = 10t$. It can be shown that when $U/t \gg 1$ or $U/t \ll 1$ the two plots coincide.

2. Two-orbital problem

In the two-orbital case, we can again diagonalize the Hamiltonian and the states are of the form $|\alpha_1\alpha_2,\beta_1,\beta_2\rangle$. Assuming $t_2 = 0$, the state $|\beta_2\rangle$ factors out and we can drop

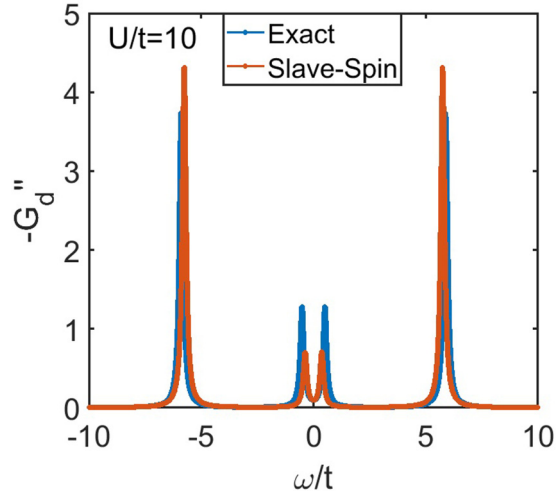

FIG. 9. A comparison of the exact vs slave-spin solutions of the single-orbital two-site problem for $U = 10t$. The smaller hybridization gap and the larger Hubbard gap are seen in the spectra. For $U \ll t$ and $U \gg t$ the two solutions agree much better than the intermediate regime shown here.

it. The remaining states depend on whether $\alpha_2 = \uparrow, \downarrow$ or $\alpha_2 = 0, 2$. In the former case, again $|\alpha_2\rangle$ factors out (does not mix):

$$\forall \alpha_2 = \uparrow, \downarrow, \quad |\alpha_1\alpha_2, \beta_1\rangle = |\alpha_2\rangle|\alpha_1, \beta_1\rangle, \tag{A14}$$

since as long as α_2 is singly occupied, the interaction is blind to the spin of α_2, and we get again the representation of Fig. 8 for each $\alpha_2 = \uparrow, \downarrow$. However, for $\alpha_2 = 0, 2$ the states mix and we find a new set of atomic states shown in Fig. 10. Each block has distinct Q^z and S^z quantum numbers. The rightmost block of Fig. 8 has the lowest energy and is the ground state (degenerate due to $\alpha_2 = \uparrow, \downarrow$). The Green's function $G_{d1}(\tau) = \langle -T d_1(\tau) d_1^\dagger \rangle$ is, therefore, as calculated before. In order to calculate $G_{d2}(\tau) = \langle -T d_2(\tau) d_2^\dagger \rangle$, we need to see which transitions are causes when $d_2^\dagger$ acts on the ground

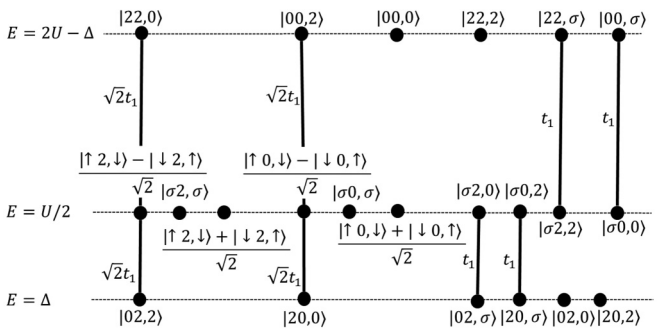

FIG. 10. A block-diagonal diagrammatic representation of the sectors of the Hamiltonian for two-orbital two-site problem, assuming $t_2 = 0$ and the second orbital, denoted by α_2 in $|\alpha_1\alpha_2, \beta_1\rangle$, is restricted to empty or fully occupied states $\alpha_2 = 0, 2$ due to the choice $t_2 = 0$. For each of the $\alpha_2 = \uparrow, \downarrow$ states, the Hamiltonian becomes a copy of single-orbital physics in Fig. 8. Again the black circles show the diagonal entries of the Hamiltonian matrix with the corresponding energy and the lines between the circles show the off-diagonal entries of the Hamiltonian.

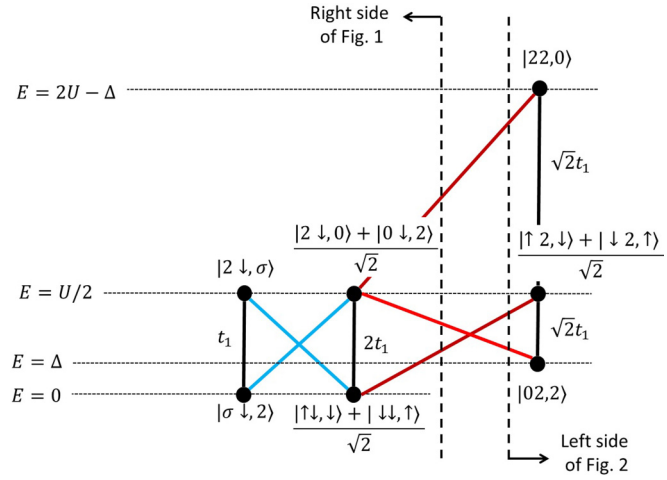

FIG. 11. A combination of Fig. 8 and Fig. 10 to highlight the ground-state (middle) block for the two-site problem. The creation operators $d_1^\dagger$ and $d_2^\dagger$ cause transitions marked in blue and red, respectively. See the main text.

state. This is shown in Fig. 11 where the right side of Fig. 8 is shown in combination with the left side of Fig. 10. Transitions caused by $d_2^\dagger$ to the states with a doublon at orbital 2 are shown in red color in this diagram. The transition caused by $d_1^\dagger$ follows the same blue arrows we had before, and therefore $G_1(\tau)$ is not modified. For $G_2(\tau)$ we have

$$G_2(\tau > 0) = -e^{-\beta\Omega}\langle\psi_g|e^{\tau H} d_{2\uparrow} e^{-\tau H} \mathbb{1} d_{2\uparrow}^\dagger|\psi_g\rangle. \tag{A15}$$

The intermediate states appearing in $\mathbb{1}$ are indicated in the figure, have energies E_n for $n = 1, 2, 3$, and are of the form

$$|\psi_n\rangle = \alpha_n|02, 2\rangle + \beta_n \frac{|\uparrow 2, \downarrow\rangle + |\downarrow 2, \uparrow\rangle}{\sqrt{2}} + \gamma_n|22, 0\rangle. \tag{A16}$$

The parameters $\alpha_n, \beta_n, \gamma_n, E_n$ have to be determined by diagonalizing the corresponding 3×3 matrix. As a result

$$G_2(\mathrm{z}) = \frac{1}{2}\sum_n \left[\frac{|m_{ng}|^2}{\mathrm{z} - (E_n - E_g)} - (\mathrm{z} \to -\mathrm{z})\right]. \tag{A17}$$

Using Eqs. (A3) and (A16) we have

$$m_{ng} = \langle\psi_n|d_{2\uparrow}^\dagger|\psi_g\rangle = \beta_n \cos\theta_g + \frac{\alpha_n + \gamma_n}{\sqrt{2}} \sin\theta_g, \tag{A18}$$

where θ_g determines the degree of the admixtures in the ground state.

Slave spin

The diagrammatic representation of the slave-spin Hamiltonian is shown in Fig. 3 with the states listed in Eq. (25). Most generally, at zero temperature the doublon part of $\Pi_2(\mathrm{z})$ is given by

$$\Pi_2(\mathrm{z}) = \frac{|m_{21,g}|^2}{\mathrm{z} - \Delta E_{21}} + \frac{|m_{22,g}|^2}{\mathrm{z} - \Delta E_{22}} + \frac{|m_{3,g}|^2}{\mathrm{z} - \Delta E_3} + (\mathrm{z} \to -\mathrm{z}),$$

where $\Delta E_n \equiv E_n - E_g$. The lowest-energy resonance is in the first term. Keeping only that term and writing both doublon

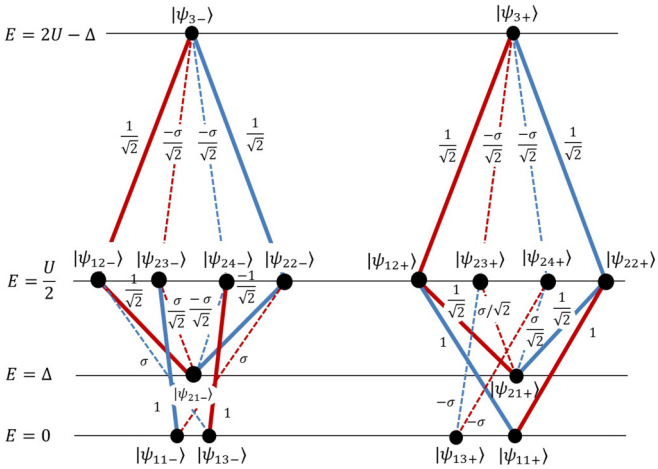

FIG. 12. A representation of the atomic states of the slave-spin Hamiltonian. The blue/red lines are transitions caused by $\tau^x_{1\sigma}$ and $\tau^x_{2\sigma}$, respectively, with amplitudes indicated. The dashed lines have an amplitude with a sign that depends on σ and they all drop out in the paramagnetic phase of the Hamiltonian.

and holon contributions we have

$$\Pi(z) = |m_{+2,g}|^2 \left[\frac{1}{z - \Delta E_{21}} - \frac{1}{z + \Delta E_{21}} \right]. \tag{A19}$$

APPENDIX B: DIAGONALIZING THE SLAVE-SPIN HAMILTONIAN

Using the notation

$$|\uparrow_1\rangle = |\Uparrow_{1\uparrow}\, \Downarrow_{1\downarrow}\rangle, \quad |2_1\rangle = |\Uparrow_{1\uparrow}\, \Uparrow_{1\downarrow}\rangle, \quad |0_1\rangle = |\,\Downarrow_{1\uparrow}\Downarrow_{1\downarrow}\rangle,$$

a simplified choice of basis for atomic states is given by

$$|\psi_{11\pm}\rangle = \frac{|\uparrow_1\rangle + |\downarrow_1\rangle}{\sqrt{2}} \frac{|\uparrow_2\rangle \pm |\downarrow_2\rangle}{\sqrt{2}}, \tag{B1}$$

$$|\psi_{13\pm}\rangle = \frac{|\uparrow_1\rangle - |\downarrow_1\rangle}{\sqrt{2}} \frac{|\uparrow_2\rangle \mp |\downarrow_2\rangle}{\sqrt{2}}, \tag{B2}$$

$$|\psi_{12\pm}\rangle = \frac{|2_1\rangle \pm |0_1\rangle}{\sqrt{2}} \frac{|\uparrow_2\rangle + |\downarrow_2\rangle}{\sqrt{2}}, \tag{B3}$$

$$|\psi_{22\pm}\rangle = \frac{|\uparrow_1\rangle + |\downarrow_1\rangle}{\sqrt{2}} \frac{|2_2\rangle \pm |0_2\rangle}{\sqrt{2}}, \tag{B4}$$

$$|\psi_{23\pm}\rangle = \frac{|2_1\rangle \mp |0_1\rangle}{\sqrt{2}} \frac{|\uparrow_2\rangle - |\downarrow_2\rangle}{\sqrt{2}}, \tag{B5}$$

$$|\psi_{24\pm}\rangle = \frac{|\uparrow_1\rangle - |\downarrow_1\rangle}{\sqrt{2}} \frac{|2_2\rangle \mp |0_2\rangle}{\sqrt{2}}, \tag{B6}$$

$$|\psi_{21\pm}\rangle = \frac{|2_1\rangle|0_2\rangle \pm |0_1\rangle|2_2\rangle}{\sqrt{2}}, \tag{B7}$$

$$|\psi_{3\pm}\rangle = \frac{|2_1\rangle|2_2\rangle \pm |0_1\rangle|0_2\rangle}{\sqrt{2}}, \tag{B8}$$

and their energies are shown in the vertical axis in Fig. 12. The transitions caused by acting on these atomic states with $\tau^x_{1\sigma}$ and $\tau^x_{2\sigma}$ are indicated in blue and red, respectively, with the indicated amplitudes. Since the kinetic Hamiltonian $a_r \tau^x_{r\sigma}$ has equal amplitudes for $\sigma = \uparrow, \downarrow$, the dashed lines cancel each other and they drop out.

For the purpose of the paper note that when $t_2 = 0$ or $a_2 = 0$, all the red lines (as well as all the blue dashed lines) drop out and the Hamiltonian becomes a doubly degenerate (plus and minus sectors) version of Fig. 3. Moreover, a chemical potential μ couples the two sectors.

APPENDIX C: SPECTRAL REPRESENTATION OF G_d

Equation (6) in the real frequency reads

$$G''_d(\omega) = -\int \frac{dx}{\pi} G''_f(\omega - x)\Pi''(x)[f(\omega - x) + n_B(-x)],$$

where $G''(\omega) \equiv \mathrm{Im}[G(\omega + i\eta]$. This can be combined with Eq. (8), but to go to zero temperature, we need to separate out the wave-function normalization part. Assuming that the slave-spin Hamiltonian has a nondegenerate ground state, the resulting spectrum at zero temperature is

$$\begin{aligned} G''_d(\omega) = {} & Z G''_f(\omega) \\ & + \sum_{n \neq g} [G''_f(\omega + \Delta E_n)\theta(-\omega > \Delta E_n)|\langle n|z_\alpha|g\rangle|^2 \\ & + G''_f(\omega - \Delta E_n)\theta(\omega > \Delta E_n)|\langle g|z_\alpha|n\rangle|^2]. \end{aligned} \tag{C1}$$

Here, $\Delta E_n = E_n - E_g$ and the ground state is treated separately and excluded from the summation.

[1] A. Georges, G. Kotliar, W. Krauth, and M. J. Rozenberg, Rev. Mod. Phys. **68**, 13 (1996).
[2] G. Kotliar and A. E. Ruckenstein, Phys. Rev. Lett. **57**, 1362 (1986).
[3] F. Lechermann, A. Georges, G. Kotliar, and O. Parcollet, Phys. Rev. B **76**, 155102 (2007).
[4] L. de' Medici, A. Georges, and S. Biermann, Phys. Rev. B **72**, 205124 (2005).
[5] A. Koga, N. Kawakami, T. M. Rice, and M. Sigrist, Phys. Rev. B **72**, 045128 (2005).
[6] E. A. Winograd and L. de' Medici, Phys. Rev. B **89**, 085127 (2014).
[7] R. Yu and Q. Si, Phys. Rev. Lett. **110**, 146402 (2013).
[8] Y. Komijani and G. Kotliar, Phys. Rev. B **96**, 125111 (2017).
[9] A. Liebsch, Phys. Rev. Lett. **91**, 226401 (2003).
[10] A. Liebsch, Europhys. Lett. **63**, 97 (2003).
[11] M. Ferrero, F. Becca, M. Fabrizio, and M. Capone, Phys. Rev. B **72**, 205126 (2005).
[12] T.-L. Dao, M. Ferrero, P. S. Cornaglia, and M. Capone, Phys. Rev. A **85**, 013606 (2012).
[13] Y. Núñez-Fernández, G. Kotliar, and K. Hallberg, Phys. Rev. B **97**, 121113(R) (2018).
[14] Y. Núñez Fernández and K. Hallberg, Front. Phys. **6**, 13 (2018).
[15] D. J. García, K. Hallberg, and M. J. Rozenberg, Phys. Rev. Lett. **93**, 246403 (2004).
[16] S. Zhou, Y. Wang, and Z. Wang, Phys. Rev. B **89**, 195119 (2014).

[17] S.-S. B. Lee, J. von Delft, and A. Weichselbaum, Phys. Rev. Lett. **119**, 236402 (2017).
[18] S.-S. B. Lee, J. von Delft, and A. Weichselbaum, Phys. Rev. B **96**, 245106 (2017).
[19] A. B. Shick, J. Kolorenc, J. Rusz, P. M. Oppeneer, A. I. Lichtenstein, M. I. Katsnelson, and R. Caciuffo, Phys. Rev. B **87**, 020505 (2013).
[20] A. B. Shick, L. Havela, A. I. Lichtenstein, and M. I. Katsnelson, Sci. Rep. **5**, 15429 (2015).
[21] C.-H. Yee, G. Kotliar, and K. Haule, Phys. Rev. B **81**, 035105 (2010).
[22] K. Haule, C.-H. Yee, and K. Kim, Phys. Rev. B **81**, 195107 (2010).
[23] A. Rüegg, S. D. Huber, and M. Sigrist, Phys. Rev. B **81**, 155118 (2010).
[24] S. Florens and A. Georges, Phys. Rev. B **70**, 035114 (2004).
[25] S. R. Hassan and L. de' Medici, Phys. Rev. B **81**, 035106 (2010).
[26] T. A. Costi, J. Kroha, and P. Wölfle, Phys. Rev. B **53**, 1850 (1996).
[27] K. Haule, S. Kirchner, J. Kroha, and P. Wölfle, Phys. Rev. B **64**, 155111 (2001).
[28] R. Nandkishore, M. A. Metlitski, and T. Senthil, Phys. Rev. B **86**, 045128 (2012).
[29] R. Žitko and M. Fabrizio, Phys. Rev. B **91**, 245130 (2015).
[30] L. de' Medici and M. Capone, Modeling many-body physics with slave-spin mean-field: Mott and Hund's physics in Fe superconductors, in *The Iron Pnictide Superconductors: An Introduction and Overview* (Springer International Publishing, Cham, 2017), pp. 115–185.
[31] W. F. Brinkman and T. M. Rice, Phys. Rev. B **2**, 4302 (1970).
[32] A. C. Hewson, *The Kondo Problem to Heavy Fermions* (Cambridge University Press, Cambridge, 1997).